



Lab on a Chip

Thermal considerations for microswimmer trap-and-release using standing surface acoustic waves

| | |
|-------------------------------|---|
| Journal: | <i>Lab on a Chip</i> |
| Manuscript ID | LC-ART-03-2021-000257.R1 |
| Article Type: | Paper |
| Date Submitted by the Author: | 03-May-2021 |
| Complete List of Authors: | Cui, Mingyang; Washington University in Saint Louis, Mechanical Engineering & Materials Science Kim, Minji; Washington University in Saint Louis, Mechanical Engineering & Materials Science Weisensee, Patricia; Washington University in St. Louis, Mechanical Engineering & Materials Science Meacham, J.; Washington University in Saint Louis, Mechanical Engineering and Materials Science |
| | |

SCHOLARONE™
Manuscripts

ARTICLE

Thermal considerations for microswimmer trap-and-release using standing surface acoustic waves

Mingyang Cui, Minji Kim, Patricia B. Weisensee, and J. Mark Meacham*

Received 00th January 20xx,
Accepted 00th January 20xx

DOI: 10.1039/x0xx00000x

Controlled trapping of cells and microorganisms using substrate acoustic waves (SAWs; conventionally termed surface acoustic waves) has proven useful in numerous biological and biomedical applications owing to the label- and contact-free nature of acoustic confinement. However, excessive heating due to vibration damping and other system losses potentially compromises the biocompatibility of the SAW technique. Herein, we investigate the thermal biocompatibility of polydimethylsiloxane (PDMS)-based SAW and glass-based SAW [that supports a bulk acoustic wave (BAW) in the fluid domain] devices operating at different frequencies and applied voltages. First, we use infrared thermography to produce heat maps of regions of interest (ROI) within the aperture of the SAW transducers for PDMS- and glass-based devices. Motile *Chlamydomonas reinhardtii* algae cells are then used to test the trapping performance and biocompatibility of these devices. At low input power, the PDMS-based SAW system cannot generate a large enough acoustic trapping force to hold swimming *C. reinhardtii* cells. At high input power, the temperature of this device rises rapidly, damaging (and possibly killing) the cells. The glass-based SAW/BAW hybrid system, on the other hand, can not only trap swimming *C. reinhardtii* at low input power, but also exhibits better thermal biocompatibility than the PDMS-based SAW system at high input power. Thus, a glass-based SAW/BAW device creates strong acoustic trapping forces in a biocompatible environment, providing a new solution to safely trap active microswimmers for research involving motile cells and microorganisms.

Introduction

Microfluidic separation, sorting, and trapping are prevalent in the fields of genetic analysis, molecular and cellular biology, biotechnology, and pharmaceuticals.¹⁻⁵ Methods that exploit microfluidics provide improved performance while reducing cost through increased flexibility, decreased sample volume and operating time, and opportunities for process automation. Technologies are classified based on their underlying physics, and optical,^{6, 7} hydrodynamic,⁸⁻¹¹ dielectrophoretic,¹²⁻¹⁵ magnetic,¹⁶⁻¹⁹ and acoustic²⁰⁻²² manipulation of cells and particles are well-established. Among these approaches, acoustic microfluidics permits label-free cell manipulation without direct contact, which minimizes undesirable surface interactions and limits physical stress on sensitive biological samples. These attributes have driven the adoption of acoustofluidic devices as research tools for single-cell and multi-cell population-based analyses.²³⁻²⁶

In conventional acoustophoresis, a standing wave is generated inside a microfluidic channel, and the acoustic radiation force arises due to scattering of the acoustic wave on suspended particles. Neglecting interparticle and particle-wall interactions, particle motion is dictated by the balance of fluidic

drag and the acoustic radiation force, which is a function of particle size and the acoustophysical properties of the particle (i.e., particle density and compressibility relative to the suspension medium).²⁷⁻³⁰ Commonly, a standing bulk acoustic wave (BAW) forms when a piezoelectric element actuates a rigid microfluidic channel (e.g., silicon/glass) at one of its resonant frequencies.³¹⁻³³ Alternatively, interdigital transducers (IDTs) can be used to generate a substrate acoustic wave (SAW) on a piezoelectric element, with the wave leaking into the fluid at the location of the microchannel.³⁴⁻³⁶ Here, we apply the conventional abbreviation SAW to include any substrate waves excited using IDTs, e.g., Rayleigh surface acoustic waves, as well as Lamb waves that arise due to the use of thin piezoelectric substrates. Typical 500- μm thick lithium niobate (LiNbO_3) substrates limit production of true Rayleigh SAW to frequencies above 40 MHz, though many researchers label such devices as SAW (meaning Rayleigh SAW) when operating in the 10-30 MHz range.³⁷ In the present work, cell trapping resulting from Lamb wave actuation should be indistinguishable from that due to Rayleigh SAW; however, Lamb wave reflection from the backside of the substrate represents an additional energy loss mechanism.

Both BAW and SAW are widely employed for particle and cell manipulation, and in most cases, the particles and cells are inactive (i.e., non-swimming).^{31, 36, 38} Demonstrations include separation of circulating tumor cells (CTCs) from white blood cells (WBCs),²⁴ single cell per well patterning of individual human lymphocytes and red blood cells,³⁹ platelet enrichment from whole blood,⁴⁰ removal of adherent cells from culture

Department of Mechanical Engineering and Materials Science, Washington University in St. Louis, St. Louis, Missouri 63130, USA.

E-mail: meachamjm@wustl.edu

† Electronic Supplementary Information (ESI) available: movies of microswimmer trap-and-release experiments. See DOI: 10.1039/x0xx00000x

plates,⁴¹ assembly of cell aggregates for drug screening and tissue engineering applications,^{42, 43} manipulation of nanomaterials on microparticle reaction substrates,^{44, 45} and even atomization of biomolecule and cell suspensions.⁴⁶⁻⁴⁸

Fewer studies report acoustic trapping and analysis of active matter, like swimming cells. Particles with their own intrinsic motors generate an additional propulsive force that the acoustic radiation force must overcome to hold the particle (cell or organism) in place. Further, the motility of microswimmers can also affect the rheological properties of the suspension medium, evidencing the complex interplay of fluidic and particle behaviors in such systems.⁴⁹ Although sample safety and biocompatibility are commonly listed as advantages of acoustofluidic manipulation, the higher input power needed to achieve sufficient trapping forces may lead to device heating that can affect biological samples. Nonetheless, thermal analyses are often incomplete or absent. Ding *et al.*⁵⁰ used a dynamic SAW field for precise positioning of a swimming *Caenorhabditis elegans*, which is known to respond to thermal stimuli (e.g., entering a state of protective paralysis at elevated temperatures);⁵¹ however, the reported input power (~ 0.8 W) needed for the operation exceeded the range over which the operating temperature was evaluated (~ 0.2 W, $\sim 26^\circ\text{C}$ at 1 min; ~ 0.32 W, $\sim 30^\circ\text{C}$ at 1 min), so it is unclear if device heating played a role in this result. Miansari *et al.*⁵² extensively characterized use of SAW irradiation to induce traumatic brain injury in *C. elegans*, carefully designing experiments to avoid paralysis observed for high input power SAW excitation of sessile droplets containing the worms. Exposure time was also kept short to reduce the risk of heating effects. Takatori *et al.*⁵³ used a focused ultrasound transducer to study the swimming pressure of acoustically confined populations of active Janus particles. In these so-called single-beam acoustic tweezers, device heating can be a concern, particularly for integration with microfluidics where a high-intensity beam is required to penetrate the channel material;^{54, 55} however, thermal effects are rarely considered.⁵⁶ BAW devices have long been used for manipulation and patterning of passive particles and cells.^{38, 57, 58} More recently, Kim *et al.*^{59, 60} applied a BAW-based acoustic trap-and-release method to quantify the swimming capability of motile *Chlamydomonas reinhardtii* and its mutants. Repeat experiments were used to assess the effects of ultrasound exposure with cells confined as loose agglomerates for up to 75 s; however, thermal effects were avoided by conducting experiments on a temperature-controlled stage.

The temperature within an acoustofluidic system is elevated due to induced vibrations and the low thermal conductivity of the channel/substrate materials, among other effects. The thermal behavior of BAW devices has been studied extensively, leading researchers to implement a number of temperature control strategies;^{25, 31, 57, 58, 61-66} however, the thermal response of SAW devices is less well studied. Kondoh *et al.*⁶⁷ analyzed the temperature variation of droplets in an open SAW system while adjusting the input power and fluid viscosity. The temperature increase during a fixed time period was found to be proportional to the applied power, and also varied with viscosity. Zheng *et al.*⁶⁸ studied the heating mechanism of

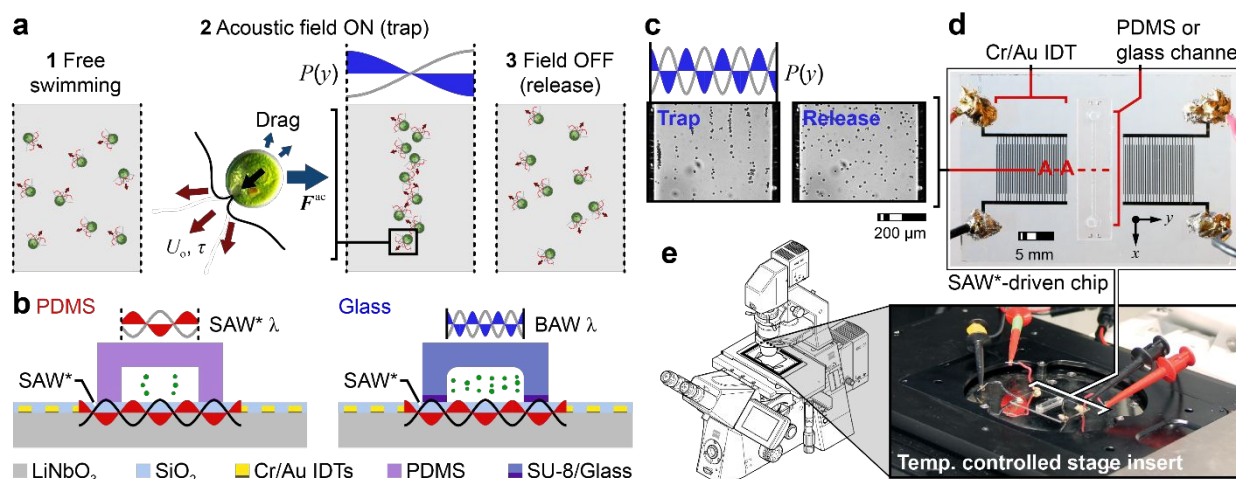
standing surface acoustic waves (SSAWs) for sessile droplets on a LiNbO₃ substrate, implicating a combination of acoustothermal effects introduced by SSAWs and Joule heating due to the alternating current field. In practice, cell manipulations are more commonly accomplished in closed polydimethylsiloxane (PDMS) channels. In addition to the role of the electric field in device heating, the temperature in such channels increases rapidly due to the high vibration damping ratio and low thermal conductivity of PDMS. Shi *et al.*³⁶ used an infrared (IR) thermometer to estimate the temperature in a closed PDMS channel for patterning cells at relatively low input power. Although device heating due to PDMS channels is typically detrimental (indeed researchers have explored alternative channel materials for this reason),⁶⁹ controlled heating can be beneficial for certain applications. Ha *et al.*⁷⁰ exploited the rapid temperature rise in higher-power SAW-driven PDMS microfluidic channels to regulate the temperature during a two-step continuous flow polymerase chain reaction (CFPCR) for DNA amplification. Their results provide the most complete description of acoustothermal effects in PDMS microchannels to date; however, rigorous thermal analysis of closed channel SAW systems suitable for trapping biological active matter remains to be done.

Here, we first use an infrared (IR) camera to map the temperature of SAW devices incorporating either PDMS (PDMS-based SAW) or glass (glass-based SAW) microchannels. We then introduce *C. reinhardtii* cells into the channels to perform trap-and-release experiments and to assess the biocompatibility of the devices operating at different frequencies and input powers (see Fig. 1). We found it impossible to trap swimming *C. reinhardtii* cells in a PDMS microchannel without a loss of function or possibly cell death. The input power required to effectively trap the cells led to acoustothermal heating at the channel location to above the thermotolerance threshold of the *C. reinhardtii* cells (i.e., the temperature above which *C. reinhardtii* cells experience heat shock that triggers a metabolic response characterized by motility loss or cell death; $\sim 37^\circ\text{C}$).^{71, 72} Conversely, a glass-based SAW device generated sufficient trapping force without fatal heating for a time duration relevant to single-cell and population-based analyses. Thus, these results show that glass-based SAW devices can generate the high acoustic radiation force needed to manipulate swimming cells while maintaining a biocompatible environment. Although this finding is most relevant to applications involving acoustic confinement of active matter, our study highlights the importance of thermal characterization in biological applications of acoustofluidic devices.

Materials and methods

Device fabrication

The SSAW devices consisted of a 500- μm thick, 128° Y-cut, X-propagating LiNbO₃ substrate patterned with a pair of IDTs, and a microfluidic channel of PDMS or glass (Fig. 1). The IDTs were oriented perpendicular to the *x*-axis of the LiNbO₃. Metal layers (Cr/Au, 10 nm/80 nm) were deposited using thermal



*Note that here SAW describes “substrate acoustic waves” (and not surface acoustic waves) to reflect the generation of Lamb waves in 500- μm thick lithium niobate substrates driven at frequencies <40 MHz.

Fig. 1 Trap-and-release illustration and mechanisms of PDMS-based and glass-based SAW device operation. (a) A standing acoustic field first traps (acoustic field on) and then releases (field off) *C. reinhardtii* cells. When trapped, the acoustic radiation force F^{ac} balances the swimming capability of the cells (characterized by a swimming velocity U_0 and reorientation time τ). (b) PDMS-based SAW device mechanism: standing substrate acoustic waves (SSAWs) leak into the fluid channel and generate standing waves; glass-based SAW device mechanism: SSAWs leak into the fluid chamber and generate standing bulk acoustic waves (SBAWs). (c) Acoustic trap-and-release experiment in a glass-based SAW device. (d) Top-view of a glass-based SAW device. (e) Device mounted on a temperature-controlled stage insert. Note that temperature control is *not* used during the current trap-and-release experiments to assess the effect of temperature rise on cell viability.

evaporation (306 Vacuum Coater, Edwards) followed by a standard lift-off process. All IDTs had 25 pairs of straight electrodes. Different devices were designed for operation at ~ 10 MHz (400 μm wavelength) and ~ 24 MHz (160 μm). Although the relatively thin electrodes raised concerns regarding ohmic heating at the IDTs, the impedance was consistently measured to be $\sim 60 \Omega$ and $\sim 76 \Omega$ for ~ 10 MHz and ~ 24 MHz devices, respectively, over the entire range of drive voltage (5–25 V_{pp} corresponding to input power of ~ 0.05 –1.2 W with slightly lower power for the higher frequency devices, see Experimental Setup). Thus, the impedance was below 100 Ω at each resonance, limiting heating at the IDTs. The aperture of the IDTs was 7 mm, and the distance between opposing IDTs was 7.9 mm. Electrodes were insulated using a 220 nm thick silicon dioxide (SiO₂) layer deposited by physical vapor deposition (PVD 75, Kurt J. Lesker). The LiNbO₃ wafer was cut to size (DAD 323, Disco).

PDMS and glass channels were 15 mm long, 545 μm wide, and 50 μm high. For consistency, all glass and PDMS channel superstrates were 20 mm long, 5 mm wide, and 1.5 mm high.⁷³ PDMS superstrates were fabricated by standard SU-8 photolithography and replica molding. A 50 μm thick layer of SU-8 2050 photoresist (MicroChem) was patterned using vendor-recommended parameters, and the resulting mold was treated with silane vapor (1H, 1H, 2H, 2H-perfluorooctyl-trichlorosilane, Sigma-Aldrich, USA) under vacuum for 2 hrs to aid in channel release. PDMS replicas (Sylgard 184, 10:1 base:cross linker, Dow) were cured at room temperature on a leveled air table for 48 hours. Cured PDMS channels were cut to final dimensions, and 1 mm diameter inlet and outlet holes were added using a biopsy punch. The glass channels were wet etched into a 1.5 mm thick soda lime glass blank, as described previously.⁷⁴ Inlet and outlet holes (1 mm diameter) were

manually drilled into the channels, and the blank was diced into 20 mm \times 5 mm pieces (DAD 323, Disco).

The PDMS channels and LiNbO₃ were treated with oxygen plasma before bonding. 10 μL of 70% ethanol was dropped onto the LiNbO₃ surface to serve as a lubricant during alignment of markers on the channel superstrate and LiNbO₃. After alignment, the ethanol was removed under vacuum, and the assembly was baked in an oven at 65°C overnight. The glass channels were bonded to the LiNbO₃ substrate by SU-8 2005 (MicroChem) using a stamp-and-stick (SAS) method.⁷⁵ Special care was taken to avoid air bubble formation and SU-8 leakage into the channel.

For select samples, an 8 μm thick black paint (Black enamel 1149TT, Testor's) layer was spin-coated onto the LiNbO₃ to facilitate accurate temperature measurement using an IR camera. For thermal characterization, the SAS method was again used to bond both PDMS and glass channels to the LiNbO₃ via liquid PDMS and SU-8 2005, respectively.

Cell culture and preparation

Wild-type (CC-125) *Chlamydomonas reinhardtii* cells were obtained from the Dutcher Lab at Washington University in St. Louis. Cells were cultured on agar plates under constant room lighting at 25°C, following a previously-reported protocol.⁷⁶ Three hours prior to an experiment, cells were resuspended in a test tube containing a medium that lacked nitrogen (adapted from Medium I of Sager and Granick⁷⁷) to promote gametogenesis. To maintain cell viability during resuspension, tubes were turned at 10 rpm using a rotator (Rotator Genie SI-2110, Scientific Industries). The tubes were vortexed to obtain a uniform suspension of cells. Typical cell concentrations were 5 – 6×10^6 cells per mL for trap-and-release experiments. Note that *C. reinhardtii* prefer environments between 20 and 32°C;

cell function and/or viability are compromised at temperatures exceeding 37–43°C, depending on cell growth conditions.^{71, 78, 79}

Experimental setup

A function generator (33522A, Agilent) and amplifiers (240L for ~10 MHz actuation, ENI; 125A250 for ~24 MHz actuation, Amplifier Research) were used to drive the SAW devices. A PC oscilloscope (PicoScope 5444D, Pico Technology) was used to determine the impedance response by measuring the applied voltage waveform (using a voltage probe at the piezoelectric element), the current waveform (voltage probe across a ground-side current sensing resistor), and phase (relationship between the two waveforms) over the relevant frequency range of interest. The nominal operating frequency was determined from the reflection coefficient.^{80, 81} *C. reinhardtii* cells were then loaded into PDMS or glass channels, and the frequency corresponding to maximum nodal confinement of the cells was identified as the optimal resonant frequency (9.62 MHz for the ~10 MHz device and 24.05 MHz for the ~24 MHz device). The input voltage range for the study was $V = 5\text{--}25 V_{pp}$, in increments of $5 V_{pp}$ (corresponding to input powers of 0.05–1.2 W and 0.04–1.1 W for the ~10 MHz and ~24 MHz devices, respectively). Each experiment was repeated three times.

Video microscopy

The trap-and-release of *C. reinhardtii* cells was visualized on the stage of an inverted microscope (Axio Observer z.1, Zeiss) using a 10× objective (EC Plan-Neofluar 10×/0.30 M27, Zeiss) (Fig. 1e). Videos were recorded at 38 frames per second (fps) at 1932 × 1460-pixel resolution (0.454 μm × 0.454 μm per pixel), using a 3-Megapixel camera and imaging software (Axiocam 503; ZEN software, Zeiss). To reduce the adhesion of cells to the channel walls, microfluidic channels were pretreated with 0.5% (w/v) bovine serum albumin (BSA) (Sigma-Aldrich) in phosphate-buffered saline (PBS) for 15 min. The microfluidic channels were flushed with DI water after each experiment to ensure that no cells remained to contaminate subsequent experiments. In addition, the time interval between each experiment was at least ten minutes, long enough to ensure that the microfluidic channels fully cooled to room temperature. A custom Python program was used to precisely control experimental inputs.

Infrared imaging and analysis

Thermal characterization experiments were performed using a custom infrared (IR) thermography setup. Devices were mounted in a laser-cut acrylic holder above a gold mirror that directed light to an IR camera (3–5.4 μm; Fast M3K, TEL-5358, Telops) with a 1× objective (TEL-5329, Telops) (Fig. 2). The black paint increased the emissivity of the substrate-channel interface to greater than 0.98 to improve temperature measurement accuracy at the location of interest.^{82–86} Videos were recorded at 20 fps and 320 × 256-pixel resolution (30 μm × 30 μm per pixel), using the IR camera and Reveal IR imaging software (Telops). The IR camera measurement was calibrated using a resistance temperature detector (PT 100, Omega) to account for the deviation from black body emission of the black paint and transmission losses in the LiNbO₃ substrate.^{85, 86} The

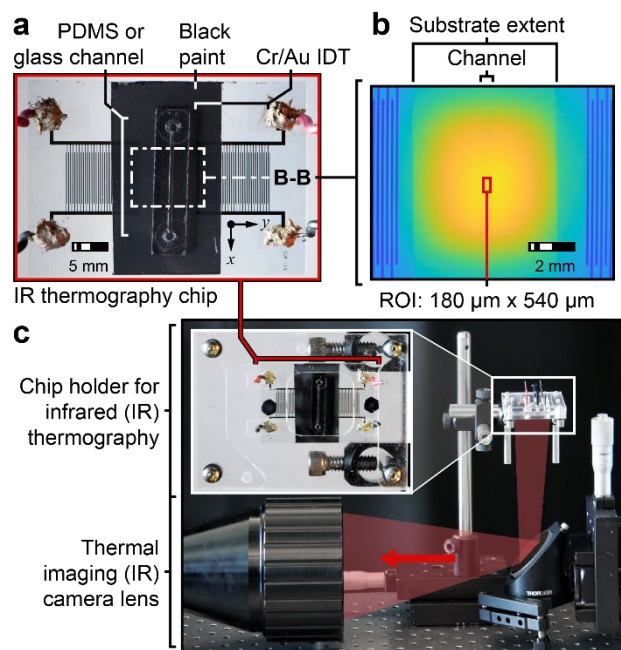


Fig. 2 Infrared (IR) thermography experimental setup. (a) Top view of a glass-based SAW device with black paint (BP). (b) A bottom-view IR image of a PDMS-based channel during actuation. The region of interest (ROI) inside the channel is 180 μm × 540 μm. (c) The custom assembly used for temperature measurements.

recorded videos and associated data were post-processed in MATLAB using the calibration. Room temperature remained at 23°C throughout. Note that the device temperatures were measured at the substrate-channel and substrate-PDMS/glass interfaces.

The thermal responses of devices with and without black paint were compared to determine whether black paint (BP) was needed to obtain accurate measurements. Channels were loaded with cell medium and the average temperature of the region of interest (180 μm × 540 μm rectangular area in the channel near the middle of the IDT aperture, labeled T_{ROI} in Fig. 2b) was monitored over a 120 s heating/recovery cycle (30 s actuation at $25 V_{pp}$, 90 s recovery). Trend lines (exponential rise/decay) were fitted to three repeats of each experimental condition (PDMS, no BP; PDMS, BP; glass, no BP; glass, BP). Thermal response plots include exponential rise/decay fits with 95% confidence bands. PDMS-based SAW devices without black paint had similar responses as those with paint showing a maximum temperature difference of 2–3°C for the ~24 MHz device (Fig. 3a). In contrast, the temperature of the glass-based SAW devices without black paint was much higher than for those with paint (Fig. 3b). For the ~10 MHz device, the maximum measured temperature was 20°C lower for the device with black paint, while the difference in measured temperature was 7°C for the ~24 MHz device. These results confirmed that black paint was needed for the reported experiments as PDMS is nearly opaque to IR radiation, while glass is not (note that LiNbO₃ is largely transparent in the near- and mid-IR range up to a wavelength of ~5 μm).

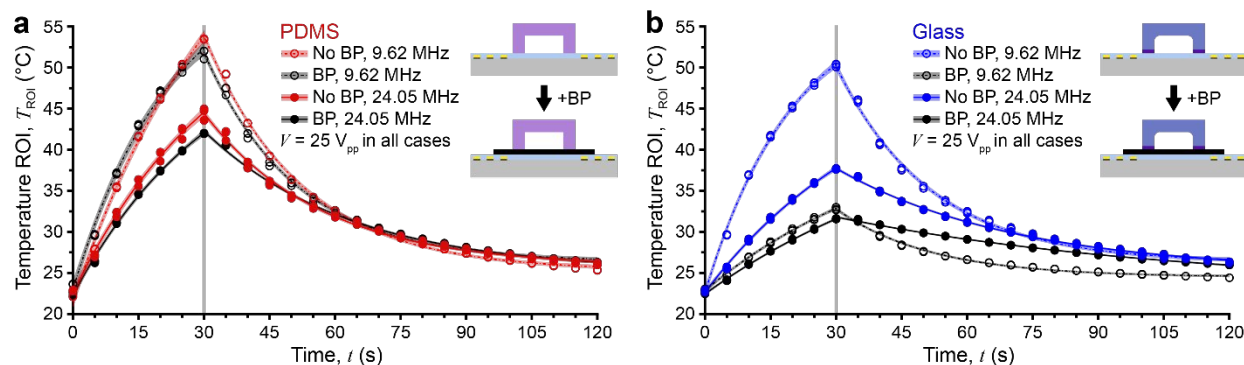


Fig. 3 Comparison of the thermal response within the ROI for uncoated devices and devices with BP when the channel is loaded with cell medium. (a) PDMS-based SAW device comparison. (b) Glass-based SAW device comparison. Experimental duration is 120 s, 30 s with the signal on and 90 s off.

Results and discussion

Heating of acoustofluidic devices presents problems in biological and biomedical applications. Although thermal analyses have been conducted on open SAW systems (e.g., for droplets on the surface of SAW devices),^{67, 68} few studies have examined heating in closed-channel systems due to the difficulty of obtaining in-channel temperature measurements. Use of temperature-dependent fluorescent dyes is well-established in microfluidics, but this approach yields only the temperature of the fluid domain.⁸⁷ Applicability is also dependent upon dye-channel compatibility and sophisticated acquisition equipment.⁸⁸ Researchers have also incorporated surface micromachined resistance temperature detectors (RTDs) for *in situ* measurements; however, each RTD is only a single point measurement probe so circuit layouts can be complex if many RTDs are needed.⁸⁹ Thermoresistive elements have been glued to the piezoelectric transducer of BAW devices to monitor global temperature transients, but again, this method provides the temperature at a single location relatively far from the microfluidic channel.³¹

In the present study, we first used IR thermography to generate heat maps of PDMS- and glass-based SAW devices driven for 30 s at voltages from 5 to 25 V_{pp} in 5 V_{pp} increments. Measurements continued for 90 s during recovery to room temperature for a total experimental time of 120 s (30 s on, 90 s off). IR thermography was selected to provide temperature information from both the microchannel and the interface between the $LiNbO_3$ substrate and channel superstrate adjacent to the microchannel. After completing the abiotic thermal characterization of both channel materials, we correlated the temperature information to the observed behaviors of swimming *C. reinhardtii* cells under the same conditions. Experiments were duplicated for ~ 10 MHz and ~ 24 MHz devices.

Thermal response of 10 MHz devices

Figure 4 details the thermal response of a PDMS-based device operated at $f = 9.62$ MHz. In the signal-on period, the system temperature increased gradually over time for all drive voltages with significant heating ($>10^\circ C$ increase in T_{ROI} at 30 s) observed for $V = 20 V_{pp}$ and $25 V_{pp}$. At $5 V_{pp}$ and $10 V_{pp}$, the T_{ROI} changed less than $5^\circ C$. An input voltage of $15 V_{pp}$ appears to represent

the maximum allowable voltage for biocompatibility with *C. reinhardtii* as T_{ROI} reached $33^\circ C$ at 30 s, just under the thermotolerance threshold of the cells (Fig. 4b). At $20 V_{pp}$ and $25 V_{pp}$, the T_{ROI} exceeded $37^\circ C$ at 20 s and 10 s, respectively, with a maximum T_{ROI} of $53^\circ C$ achieved at the end of the $25 V_{pp}$ actuation period.

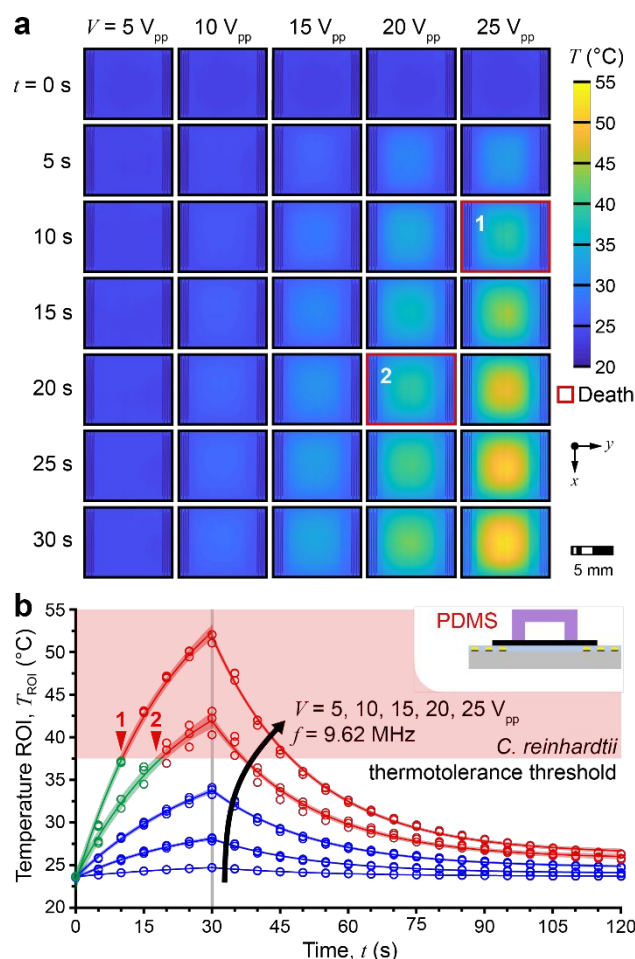


Fig. 4 Heat maps of a 10 MHz PDMS-based SAW device (experimental actuation frequency $f = 9.62$ MHz). (a) The thermal response of the region between the IDTs for different drive voltages ($V = 5\text{--}25 V_{pp}$). Cases highlighted in red indicate possible cell death due to heat stress. (b) Progression of the ROI temperature T_{ROI} for different drive voltages. The *C. reinhardtii* thermotolerance threshold ($T \approx 37^\circ C$) is shown for reference.

Heat maps also indicate that the ‘hot spot’ extends along most of the microchannel length within the aperture of the IDTs, and well into the PDMS superstrate bounding the channel in this region. Here, the interface between the LiNbO₃ substrate and PDMS channel heats quickly. The PDMS superstrate outside the aperture is cooler due to a lower amplitude of the SSAW outside the aperture and potentially because heat conduction within the PDMS is poor. In addition, the LiNbO₃ outside of the PDMS superstrate remains relatively cool regardless the applied voltage, as there is little attenuation of the travelling SAW before it reaches the PDMS layer.

The glass-based device and a SAW device without a bonded channel were also tested at the same frequencies and applied voltages as the PDMS-based device. The rise and fall of T_{ROI} for the three different devices driven at 25 V_{pp} are shown in Fig. 5a. The T_{ROI} of the glass-based SAW device stays below the thermotolerance threshold of the *C. reinhardtii* cells, and the T_{ROI} of the no-channel SAW device barely increases. The glass channel superstrate is less attenuating than the PDMS. In addition, PDMS has a significantly lower thermal conductivity than glass (0.15 W/m-K vs. 1.3–1.5 W/m-K). Thus, heat generated at the interface of the LiNbO₃ and channel superstrate was dissipated more easily in glass than in PDMS-based devices.

Based on the thermal response of the 10 MHz PDMS-based SAW device, we conclude that it is difficult to maintain a thermally biocompatible environment for *C. reinhardtii* at high input voltage without an active cooling system. If possible, acoustic trapping of *C. reinhardtii* cells would have to occur at a drive voltage of less than 15 V_{pp} in a PDMS-based device. No such restriction exists for the 10 MHz glass-based device.

C. reinhardtii trap-and-release in 10 MHz devices

To confirm the range of biocompatibility predicted by the IR thermography, we conducted a series of acoustic trap-and-release experiments for the ~10 MHz devices loaded with *C. reinhardtii* cells. For the PDMS-based device operated at $f = 9.62$ MHz, $V = 5$ –15 V_{pp}, the acoustic radiation force was not large enough to overcome the intrinsic swimming capability of the cells, and cells did not become confined to nodal lines of the acoustic field. At 20 V_{pp}, *C. reinhardtii* cell alignment was observed after approximately 20 s of actuation; however, it was clear that cell trapping was due to a loss of motility (or cell death) and not to acoustic confinement against the swimming force. Cells were not only held in nodal bands distributed in the y -direction across the channel, but they also ceased swimming in the x -direction along the channel length. Similar behavior was seen at an operating voltage of 25 V_{pp}, with cells quickly focusing to the nodes in 10–12 s (Fig. 6a and Supplementary Movie S1). Referring to Fig. 4, the elapsed time to motility loss closely corresponded to the time required for T_{ROI} to reach 37°C, the *C. reinhardtii* thermotolerance threshold. For both the 20 V_{pp} and 25 V_{pp} cases, the cells remained at nodes after the signal was turned off, further confirming the loss of viability (see ‘Release’ in Fig. 6a and Supplementary Movie S1). The power required to generate a sufficient acoustic radiation force to trap the swimming cells resulted in device overheating that

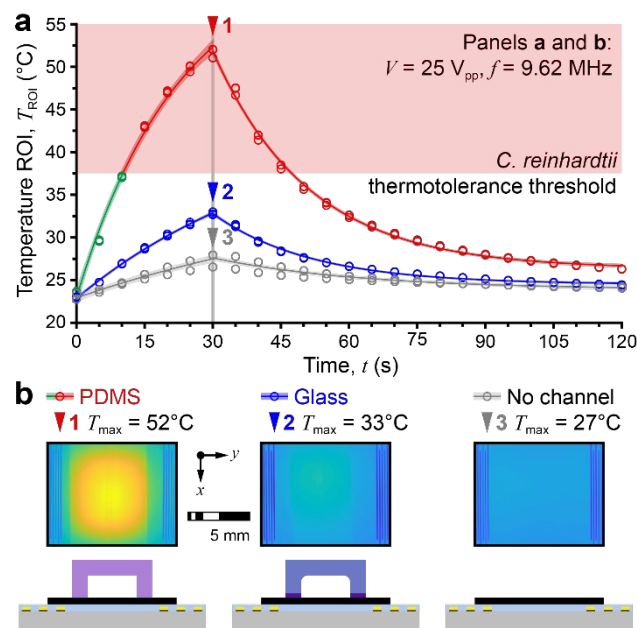


Fig. 5 Progression of T_{ROI} for PDMS-based SAW, glass-based SAW, and no-channel SAW devices. (a) The T_{ROI} of glass-based SAW and no-channel SAW are under the *C. reinhardtii* thermotolerance threshold throughout the experiment. (b) Heat maps at 30 s, the time of maximum device temperature.

damaged the cells and effectively turned them into passive tracer particles. Thus, we conclude that the PDMS-based device is not able to trap live *C. reinhardtii* cells.

We then repeated the trap-and-release experiments using a glass-based SAW device. At 5 V_{pp} and 10 V_{pp}, no cell lines formed, suggesting that the acoustic radiation force was still too weak to overcome the swimming force. When the applied voltage was increased to 15 V_{pp}, the cells congregated at nodal lines corresponding to the acoustic half-wavelength of a standing bulk acoustic wave. At 20 V_{pp} and 25 V_{pp}, the *C. reinhardtii* cells were trapped tightly within the nodes of the standing BAW field, but cells readily dispersed after the signal was turned off (Fig. 6b and Supplementary Movie S2). These results prove that the glass-based SAW device is able to trap-and-release cells without damaging them. The glass-based device provides similar functionality to our earlier BAW trap-and-release motility assessment platform,⁵⁹ combined with the notable advantages of SAW, including higher attainable drive frequencies and a planar actuator design.^{90, 91}

Thermal response and *C. reinhardtii* trap-and-release in 24 MHz devices

To determine the applicability of our results to higher operating frequencies, we also tested PDMS- and glass-based SAW devices at a frequency of 24.05 MHz, using the same drive voltages as for the 10 MHz devices. For higher-frequency operation, the thermal environment in the PDMS channel did not exceed the *C. reinhardtii* thermotolerance threshold until the applied voltage was 25 V_{pp} (Fig. 7a). In this case, the temperature within the ROI increased to 37°C at 20 s, predicting that cell death would begin near this exposure time. In contrast,

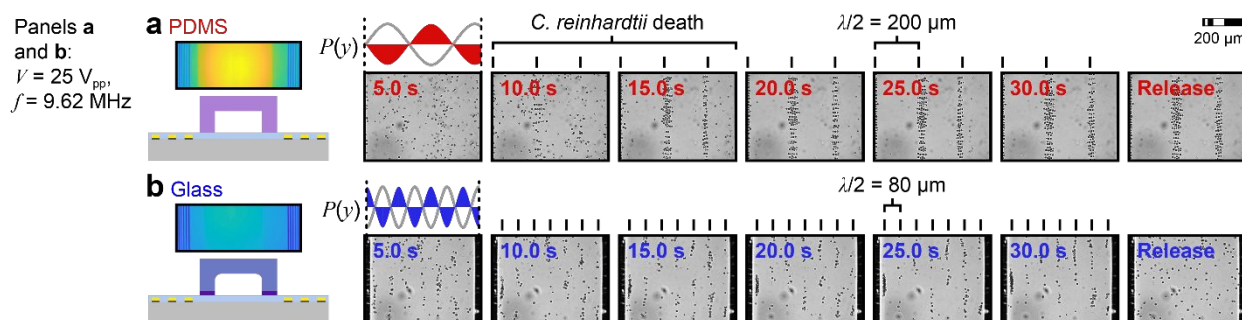


Fig. 6 Trap-and-release at 9.62 MHz and 25 V_{pp} . (a) The PDMS-based device is not able to trap swimming *C. reinhardtii* but focuses immotile cells. Immotile *C. reinhardtii* cells do not redistribute after the signal is turned off. (b) The glass-based device successfully traps live *C. reinhardtii* at SBAW nodal positions. The motile *C. reinhardtii* cells redistribute evenly throughout the channel after the signal is removed.

the temperature within the glass channel stayed below 32°C, even for the highest applied voltage of 25 V_{pp} .

We again confirmed our abiotic results using *C. reinhardtii* cell trap-and-release to assess the biocompatibility of both devices. In the 24 MHz PDMS-based device, cells were not trapped within nodal lines at drive voltages from 5–20 V_{pp} , likely due to the insufficient acoustic radiation force. At 25 V_{pp} , the cells began to lose motility at around 20 s as expected (Fig. 7b and Supplementary Movie S3). Further, higher magnification images of treated cells suggested that some cells disintegrated, and intact cells exhibited extensive blebbing and other signs of damage (see Supplementary Fig. S1). By contrast, in the 24 MHz glass-based device cell confinement began at 15 V_{pp} , with tighter trapping observed at 20 V_{pp} and 25 V_{pp} . As with the lower frequency actuation at 25 V_{pp} , the cells were trapped and then released without damage for operation at 24.05 MHz (Fig. 7c and Supplementary Movie S4). Unlike at the lower operating frequency, many cells are seen ‘hopping’ back and forth between adjacent nodal positions, which may indicate that the acoustic radiation force cannot overcome the maximum swimming force when cells are oriented perpendicular to the nodal lines, or that the trapping becomes less effective as the half wavelength approaches the size of the cells. It is also possible that for the glass-based SAW device, the BAW is not well-matched to the drive frequency of the SAW.

Interestingly, in the PDMS-based device, alignment of immotile or dead cells was observed at both nodes and what appear to be antinodes, where they remained after the removal of the applied voltage (Fig. 7b and Supplementary Movie S3). We first thought that dead cells might focus at both nodal and antinodal locations due to the three-dimensional (3D) nature of the acoustic wave field (some lines of cells are blurry suggesting that they are positioned at different focal z -depths); however, a control experiment using 10 μm poly(methyl methacrylate) (PMMA) beads verified the nodal locations at the half-wavelength of the SAW (Fig. 7b, $\lambda/2 = 80 \mu\text{m}$). Thus, it is not entirely clear why dead cells focus to both nodes and antinodes. Further investigation is needed to determine whether the dead *C. reinhardtii* cell population may have different acoustophysical properties (i.e., density and compressibility) than the live cells or if indeed the 3D wave field affects cells differently than PMMA beads (e.g., if beads settle prior to focusing unlike swimming cells that initially fill the 3D channel).

In summary, the 24 MHz PDMS-based SAW device was also not able to trap live *C. reinhardtii* cells due to a too-weak acoustic radiation force and/or lethal heating at higher input power. Dead cells were trapped in the nodal/anti-nodal lines of the SAW and remained there even after the signal was turned off. The 24 MHz glass-based SAW device successfully trapped live cells; cell confinement occurred at standing BAW nodes formed by the leaky SAW reflected between the glass walls of the fluid microchannel. The acoustic radiation force was strong enough to trap the cells prior to release, though cells were able to hop between trapping sites as the acoustic half wavelength ($\sim 30 \mu\text{m}$) became comparable to the cell-plus-cilia diameter of $\sim 20 \mu\text{m}$.

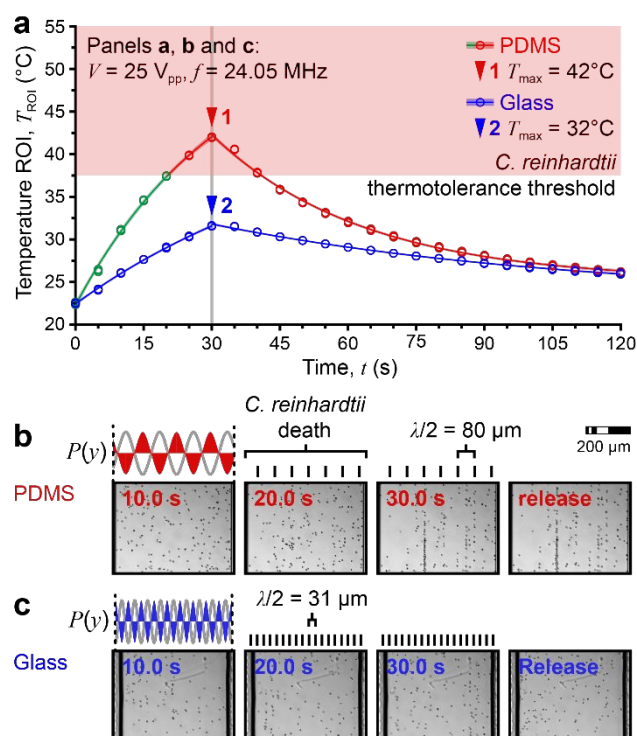


Fig. 7 Thermal response and trap-and-release are correlated for the 24 MHz device operated at 24.05 MHz and 25 V_{pp} . (a) The T_{ROI} progression of PDMS-based and glass-based SAW devices. (b) The PDMS-based device is not able to trap swimming *C. reinhardtii*, which become immotile at ~ 20 s. (c) The glass-based device is able to trap-and-release live cells.

Conclusions

Understanding the thermal transport characteristics of acoustofluidic devices is critical to their implementation, whether the goal is to control a temperature-sensitive process like PCR amplification of DNA or to mitigate potential damage to cells and biomolecules. Even for relatively low input powers where cell viability is less of a concern, biophysical and biochemical processes are affected by slight variations in temperature. For example, the swimming velocity of wild type *C. reinhardtii* (strain CC-125) grown at 25°C has been reported to vary from 42 $\mu\text{m/s}$ to 123 $\mu\text{m/s}$ in the range from 10°C to 30°C.⁹² In our laboratory, we have observed an increase in *C. reinhardtii* cell beat frequency from ~55 Hz to ~75 Hz over the smaller 15°C to 25°C range (unpublished data).

Aside from potential adverse effects on cells and biomolecules, separation and trapping performance can suffer when the operating temperature deviates significantly from the design conditions (typically room temperature). The electromechanical and acoustophysical properties of the piezoelectric substrate, channel superstrate, and liquid sample are strongly dependent on temperature. Even so, thermal effects are often neglected or considered as less important aspects of system operation. Biological studies involving manipulation of cells using SAW-based devices rarely include appropriate controls or temperature calibration protocols.

In this work, we quantify the temperature field in PDMS- and glass-based SAW devices using an IR camera, incorporating a thin black paint layer to ensure accurate temperature measurement at the microchannel-substrate interface. Heat maps for both devices indicate that significant device heating is concentrated at the microchannel near the midpoint of the IDT aperture. These abiotic measurements are correlated with biological outcomes by performing acoustic trap-and-release of *C. reinhardtii* cells. We observe a loss of viability (and likely cell death) in PDMS-based SAW devices, suggesting that in those devices it is not possible to generate a force sufficient to trap swimming cells without excessive heating due to a high input power, vibration damping characteristics, and the poor thermal transport properties of PDMS. Glass-based devices support bulk acoustic waves driven at resonance by SAW to trap *C. reinhardtii* cells at lower input power, while effectively removing generated heat to maintain a thermally biocompatible environment. Thus, glass-based SAW devices can enable investigation of cell motility, cilia function, and the cellular response to mechanical and chemical stimuli with higher precision than comparable silicon/glass BAW devices driven by bulk transducers. We reiterate that it is the device heating that damages cells in PDMS-based SAW devices and not the strength of the acoustic field, as cells cease swimming before they are focused; the glass-based devices achieve a stronger field strength to confine cells without damage as demonstrated by the free-swimming cells after removal of the field. Our results highlight the importance of rigorous thermal analysis of SAW-based devices and promote glass-based hybrid SAW/BAW as a compelling technology when high-frequency, short-wavelength ultrasonic standing waves are needed.

Conflicts of interest

There are no conflicts to declare.

Acknowledgements

This work was supported by the National Science Foundation (Grant Nos. CMMI-1633971 and CBET-1944063). The authors acknowledge partial financial support from Washington University in St. Louis and the Institute of Materials Science and Engineering for the use of fabrication instruments and staff assistance. The authors thank Susan Dutcher and Mathieu Bottier for providing *C. reinhardtii* cells. The authors also thank Boshun Gao for assistance debugging Python control code, Wenming Li for fabrication support, and James Ballard for writing consultation.

References

1. B. De Wagenaar, S. Dekker, H. L. de Boer, J. G. Bomer, W. Olthuis, A. van den Berg and L. I. Segerink, *Lab Chip*, 2016, **16**, 1514-1522.
2. T. Frank and S. Tay, *Lab Chip*, 2013, **13**, 1273-1281.
3. M. Weiss, J. P. Frohnmayer, L. T. Benk, B. Haller, J.-W. Janiesch, T. Heitkamp, M. Börsch, R. B. Lira, R. Dimova and R. Lipowsky, *Nat. Mater.*, 2018, **17**, 89.
4. Y. Zeng, R. Novak, J. Shuga, M. T. Smith and R. A. Mathies, *Anal. Chem.*, 2010, **82**, 3183-3190.
5. R. Zilionis, J. Nainys, A. Veres, V. Savova, D. Zemmour, A. M. Klein and L. Mazutis, *Nat. Protoc.*, 2017, **12**, 44.
6. X. Wang, S. Chen, M. Kong, Z. Wang, K. D. Costa, R. A. Li and D. Sun, *Lab Chip*, 2011, **11**, 3656-3662.
7. M. P. MacDonald, G. C. Spalding and K. Dholakia, *Nature*, 2003, **426**, 421.
8. M. E. Warkiani, B. L. Khoo, L. Wu, A. K. P. Tay, A. A. S. Bhagat, J. Han and C. T. Lim, *Nat. Protoc.*, 2016, **11**, 134.
9. H. W. Hou, M. E. Warkiani, B. L. Khoo, Z. R. Li, R. A. Soo, D. S.-W. Tan, W.-T. Lim, J. Han, A. A. S. Bhagat and C. T. Lim, *Sci. Rep.*, 2013, **3**, 1259.
10. K. Chung, C. A. Rivet, M. L. Kemp and H. Lu, *Anal. Chem.*, 2011, **83**, 7044-7052.
11. D. Di Carlo, N. Aghdam and L. P. Lee, *Anal. Chem.*, 2006, **78**, 4925-4930.
12. E. M. Freer, O. Grachev, X. Duan, S. Martin and D. P. Stumbo, *Nat. Nanotechnol.*, 2010, **5**, 525.
13. D.-H. Lee, X. Li, A. Jiang and A. P. Lee, *Biomicrofluidics*, 2018, **12**, 054104.
14. M. D. Vahey and J. Voldman, *Anal. Chem.*, 2008, **80**, 3135-3143.
15. H. Song, J. M. Rosano, Y. Wang, C. J. Garson, B. Prabhakarapandian, K. Pant, G. J. Klarmann, A. Perantoni, L. M. Alvarez and E. Lai, *Lab Chip*, 2015, **15**, 1320-1328.
16. M. Hejazian and N.-T. Nguyen, *Lab Chip*, 2015, **15**, 2998-3005.
17. S. Kim, S.-I. Han, M.-J. Park, C.-W. Jeon, Y.-D. Joo, I.-H. Choi and K.-H. Han, *Anal. Chem.*, 2013, **85**, 2779-2786.
18. N. Pamme and C. Wilhelm, *Lab Chip*, 2006, **6**, 974-980.
19. B. Lim, V. Reddy, X. Hu, K. Kim, M. Jadhav, R. Abedini-

- Nassab, Y.-W. Noh, Y. T. Lim, B. B. Yellen and C. Kim, *Nat. Commun.*, 2014, **5**, 3846.
20. A. Riaud, M. Baudoin, O. B. Matar, L. Becerra and J.-L. Thomas, *Phys. Rev. Appl.*, 2017, **7**, 024007.
21. J. Shi, X. Mao, D. Ahmed, A. Colletti and T. J. Huang, *Lab Chip*, 2008, **8**, 221-223.
22. F. Petersson, L. Åberg, A.-M. Swärd-Nilsson and T. Laurell, *Anal. Chem.*, 2007, **79**, 5117-5123.
23. P. Li and T. J. Huang, *Anal. Chem.*, 2019, **91**, 757-767.
24. M. Wu, P. H. Huang, R. Zhang, Z. Mao, C. Chen, G. Kemeny, P. Li, A. V. Lee, R. Gyanchandani and A. J. Armstrong, *Small*, 2018, **14**, 1801131.
25. A. Urbansky, F. Olm, S. Scheding, T. Laurell and A. Lenshof, *Lab Chip*, 2019, **19**, 1406-1416.
26. C. W. Shields, C. D. Reyes and G. P. Lopez, *Lab Chip*, 2015, **15**, 1230-1249.
27. H. Bruus, *Lab Chip*, 2012, **12**, 1014-1021.
28. L. P. Gor'kov, *Sov. Phys. Dokl.*, 1962, **6**, 773-775.
29. K. Yosioka and Y. Kawasima, *Acta Acust. Acust.*, 1955, **5**, 167-173.
30. L. V. King, *Proc. R. Soc. London, Ser. A*, 1934, **147**, 212-240.
31. P. Augustsson, R. Barnkob, S. T. Wereley, H. Bruus and T. Laurell, *Lab Chip*, 2011, **11**, 4152-4164.
32. P. B. Muller, R. Barnkob, M. J. H. Jensen and H. Bruus, *Lab Chip*, 2012, **12**, 4617-4627.
33. I. Leibacher, P. Reichert and J. Dual, *Lab Chip*, 2015, **15**, 2896-2905.
34. P. R. Rogers, J. R. Friend and L. Y. Yeo, *Lab Chip*, 2010, **10**, 2979-2985.
35. G. Destgeer, B. H. Ha, J. Park, J. H. Jung, A. Alazzam and H. J. Sung, *Anal. Chem.*, 2015, **87**, 4627-4632.
36. J. Shi, D. Ahmed, X. Mao, S.-C. S. Lin, A. Lawit and T. J. Huang, *Lab Chip*, 2009, **9**, 2890-2895.
37. W. Connacher, N. Zhang, A. Huang, J. Mei, S. Zhang, T. Gopesh and J. Friend, *Lab Chip*, 2018, **18**, 1952-1996.
38. M. Antfolk, C. Antfolk, H. Lilja, T. Laurell and P. Augustsson, *Lab Chip*, 2015, **15**, 2102-2109.
39. D. J. Collins, B. Morahan, J. Garcia-Bustos, C. Doerig, M. Plebanski and A. Neild, *Nat. Commun.*, 2015, **6**, 8686.
40. C. Richard, A. Fakhfour, M. Colditz, F. Striggow, R. Kronstein-Wiedemann, T. Tonn, M. Medina-Sánchez, O. G. Schmidt, T. Gemming and A. Winkler, *Lab Chip*, 2019.
41. T. Inui, J. Mei, C. Imashiro, Y. Kurashina, J. Friend and K. Takemura, *Lab Chip*, 2021, **21**, 1299-1306.
42. X. Hu, S. Zhao, Z. Luo, Y. Zuo, F. Wang, J. Zhu, L. Chen, D. Yang, Y. Zheng and Y. Zheng, *Lab Chip*, 2020, **20**, 2228-2236.
43. X. Hu, J. Zhu, Y. Zuo, D. Yang, J. Zhang, Y. Cheng and Y. Yang, *Lab Chip*, 2020, **20**, 3515-3523.
44. M. Binkley, M. Cui, W. Li, S. Tan, M. Berezin and J. Meacham, *Phys. Fluids*, 2019, **31**, 082007.
45. M. M. Binkley, M. Cui, M. Y. Berezin and J. M. Meacham, *ACS Biomater. Sci. Eng.*, 2020, **6**, 6108-6116.
46. A. E. Rajapaksa, J. J. Ho, A. Qi, R. Bischof, T.-H. Nguyen, M. Tate, D. Piedrafita, M. P. McIntosh, L. Y. Yeo, E. Meeusen, R. Coppel and J. Friend, *Respir. Res.*, 2014, **15**, 1-12.
47. V. G. Zarnitsyn, J. M. Meacham, M. J. Varady, C. Hao, F. L. Degertekin and A. G. Fedorov, *Biomed. Microdevices*, 2008, **10**, 299-308.
48. J. M. Meacham, K. Durvasula, F. L. Degertekin and A. G. Fedorov, *Sci. Rep.*, 2018, **8**, 1-10.
- A. G. McDonnell, T. C. Gopesh, J. Lo, M. O'Bryan, L. Y. Yeo, J. R. Friend and R. Prabhakar, *Soft Matter*, 2015, **11**, 4658-4668.
50. X. Ding, S.-C. S. Lin, B. Kiraly, H. Yue, S. Li, I.-K. Chiang, J. Shi, S. J. Benkovic and T. J. Huang, *Proc. Natl. Acad. Sci. U. S. A.*, 2012, **109**, 11105-11109.
51. G. W. Stegeman, D. Medina, A. D. Cutter and W. S. Ryu, *BMC Neurosci.*, 2019, **20**, 1-12.
52. M. Miansari, M. D. Mehta, J. M. Schilling, Y. Kurashina, H. H. Patel and J. Friend, *Sci. Rep.*, 2019, **9**, 1-11.
53. S. C. Takatori, R. De Dier, J. Vermant and J. F. Brady, *Nat. Commun.*, 2016, **7**, 10694.
54. J. S. Jeong, J. W. Lee, C. Y. Lee, S. Y. Teh, A. Lee and K. K. Shung, *Biomed. Microdevices*, 2011, **13**, 779-788.
55. J. Lee, J. S. Jeong and K. K. Shung, *Ultrasonics*, 2013, **53**, 249-254.
56. X. Chen, K. H. Lam, R. Chen, Z. Chen, P. Yu, Z. Chen, K. K. Shung and Q. Zhou, *Biotechnol. Bioeng.*, 2017, **114**, 2637-2647.
57. P. Augustsson, C. Magnusson, M. Nordin, H. Lilja and T. Laurell, *Anal. Chem.*, 2012, **84**, 7954-7962.
58. E. J. Fong, A. C. Johnston, T. Notton, S.-Y. Jung, K. A. Rose, L. S. Weinberger and M. Shusteff, *Analyst*, 2014, **139**, 1192-1200.
59. M. Kim, E. Huff, M. Bottier, S. K. Dutcher, P. V. Bayly and J. M. Meacham, *Soft Matter*, 2019, **15**, 4266-4275.
60. M. Kim, P. V. Bayly and J. M. Meacham, *Lab Chip*, 2021, **21**, 521-533.
61. J. D. Adams, C. L. Ebbesen, R. Barnkob, A. H. Yang, H. T. Soh and H. Bruus, *J. Micromech. Microeng.*, 2012, **22**, 075017.
62. M. Wiklund, *Lab Chip*, 2012, **12**, 2018-2028.
63. J. J. Hawkes and W. T. Coakley, *Sens. Actuators, B*, 2001, **75**, 213-222.
64. J. J. Hawkes and W. T. Coakley, *Enzyme Microb. Technol.*, 1996, **19**, 57-62.
65. M. Evander, L. Johansson, T. Lilliehorn, J. Piskur, M. Lindvall, S. Johansson, M. Almqvist, T. Laurell and J. Nilsson, *Anal. Chem.*, 2007, **79**, 2984-2991.
66. L. Johansson, M. Evander, T. Lilliehorn, M. Almqvist, J. Nilsson, T. Laurell and S. Johansson, *Ultrasonics*, 2013, **53**, 1020-1032.
67. J. Kondoh, N. Shimizu, Y. Matsui, M. Sugimoto and S. Shiokawa, *Sens. Actuators, A*, 2009, **149**, 292-297.
68. T. Zheng, C. Wang, Q. Hu and S. Wei, *Appl. Phys. Lett.*, 2018, **112**, 233702.
69. S. M. Langelier, L. Y. Yeo and J. Friend, *Lab Chip*, 2012, **12**, 2970-2976.
70. B. H. Ha, K. S. Lee, G. Destgeer, J. Park, J. S. Choung, J. H. Jung, J. H. Shin and H. J. Sung, *Sci. Rep.*, 2015, **5**, 11851.
71. M. Schroda, D. Hemme and T. Mühlhaus, *Plant J.*, 2015, **82**, 466-480.
72. B. Xie, S. Bishop, D. Stessman, D. Wright, M. H. Spalding and L. J. Halverson, *ISME J.*, 2013, **7**, 1544-1555.
73. M. C. Jo and R. Guldiken, *Microelectron. Eng.*, 2014, **113**, 98-104.
74. M. Cui, M. Binkley, H. Shekhani, M. Berezin and J. Meacham, *Biomicrofluidics*, 2018, **12**, 034110.
75. S. Satyanarayana, R. N. Karnik and A. Majumdar, *J. Microelectromech. Syst.*, 2005, **14**, 392-399.
76. J. A. Holmes and S. K. Dutcher, *J. Cell Sci.*, 1989, **94**, 273-285.

ARTICLE

Journal Name

77. R. Sager and S. Granick, *Ann. N. Y. Acad. Sci.*, 1953, **56**, 831-838.
78. Y. Kobayashi, N. Harada, Y. Nishimura, T. Saito, M. Nakamura, T. Fujiwara, T. Kuroiwa and O. Misumi, *Genome Biol. Evol.*, 2014, **6**, 2731-2740.
79. Y. Tanaka, Y. Nishiyama and N. Murata, *Plant Physiol.*, 2000, **124**, 441-450.
80. A. Winkler, R. Brünig, C. Faust, R. Weser and H. Schmidt, *Sens. Actuators, A*, 2016, **247**, 259-268.
81. J. W. Ng, C. Devendran and A. Neild, *Lab Chip*, 2017, **17**, 3489-3497.
82. I. Golobic, J. Petkovsek, M. Baselj, A. Papez and D. Kenning, *Heat Mass Transfer*, 2009, **45**, 857-866.
83. M. Gibbons, C. Howe, P. Di Marco and A. Robinson, *J. Phys.: Conf. Ser.*, 2016, **745**, 032066.
84. M. Gibbons, P. Di Marco and A. J. Robinson, *Int. J. Heat Mass Transfer*, 2018, **121**, 641-652.
85. W. Qi, J. Li and P. B. Weisensee, *Langmuir*, 2019, **35**, 17185-17192.
86. W. Qi and P. B. Weisensee, *Phys. Fluids*, 2020, **32**, 067110.
87. D. Ross, M. Gaitan and L. E. Locascio, *Anal. Chem.*, 2001, **73**, 4117-4123.
88. A. Nakano, J. Luo and A. Ros, *Anal. Chem.*, 2014, **86**, 6516-6524.
89. S. Narayanan, A. G. Fedorov and Y. K. Joshi, 2010.
90. Z. Mao, Y. Xie, F. Guo, L. Ren, P.-H. Huang, Y. Chen, J. Rufo, F. Costanzo and T. J. Huang, *Lab Chip*, 2016, **16**, 515-524.
91. L. Johansson, J. Enlund, S. Johansson, I. Katardjiev, M. Wiklund and V. Yantchev, *J. Micromech. Microeng.*, 2012, **22**, 025018.
92. M. Sekiguchi, S. Kameda, S. Kurosawa, M. Yoshida and K. Yoshimura, *Sci. Rep.*, 2018, **8**, 1-10.